Ceramics International 46 (2020) 3644–3654

Contents lists available at ScienceDirect

Ceramics International

journal homepage: www.elsevier.com/locate/ceramint

Fracture behavior of TBCs with cooling hole structure under cyclic thermal loadings

Jishen Jiang[a,b], Di Wu[c], Weizhe Wang[b], Xiaofeng Zhao[c], Xianfeng Ma[a,*], Biao Wang[a], Hui-Ji Shi[d]

[a] Sino-French Institute of Nuclear Engineering and Technology, Sun Yat-Sen University, Zhuhai, 519082, Guangdong, China
[b] Key Laboratory of Power Machinery and Engineering, School of Mechanical and Power Engineering, Shanghai Jiao Tong University, Shanghai, 200240, China
[c] School of Material Science and Engineering, Shanghai Jiao Tong University, Shanghai, 200240, China
[d] AML, School of Aerospace, Tsinghua University, Beijing, 100084, China

ARTICLE INFO

Keywords:
Thermal barrier coating (TBC)
Cooling hole
Finite element analysis
Interfacial crack
Thermal cycling

ABSTRACT

The integrity of thermal barrier coatings (TBCs) plays an important role in the performance of turbine blades, nevertheless the effect of cooling hole on fracture of TBCs have been less studied. The present work aimed to study the stress evolution and fracture behavior of TBCs with cooling hole under cyclic thermal loadings. Cyclic thermal tests were conducted and the cracking behavior of TBCs around cooling hole was examined using scanning electron microscope (SEM). TBCs exhibited two types of cracks near the hole edge, i.e. surface crack in the top coat and interfacial crack, which could lead to local TBC spallation and shorten the TBC lifetime. To disclose the fracture mechanism, finite element (FE) analysis was also performed. The computed residual stress values were consistent with those measured by Raman spectroscopy tests. FE simulations indicated that the free-edge effect facilitated interfacial peeling and shear stresses near the cooling hole, and hence promoted the initiation of interfacial crack in TBCs. With the increase of thermal loading cycles, the interfacial crack propagated and then coalesced with the surface cracks in the top coat, leading to the final spallation of TBCs at the cooling hole.

1. Introduction

Thermal barrier coatings (TBCs) have been widely applied in gas turbine engines to protect turbine blades from hot corrosion and other damage. Although high temperature mechanical performances and fracture mechanisms of TBCs have been studied for decades, the premature failure of TBCs still be the biggest problem to limit their service lifetimes [1]. The multilayered structure of TBCs brings about huge residual stresses from the thermal mismatch between layers, which can drive interfacial delamination of TBCs. However, in service conditions, the stress state in TBCs could be more complicated. In the TBC-film cooling system of the turbine blade, the film cooling hole could be a crucial factor for the TBC failure, since it brings about huge local stress concentration around the hole. The free-edge effect of cooling hole may facilitate interfacial peeling and shear stresses, which aggravates the local stress state and even drives interfacial crack initiation in TBCs [2,3]. However, previous studies on the integrity of TBC-film cooling system were rather limited. A better understanding of the stress and failure behaviors of TBCs adjacent to the cooling hole is highly desirable to evaluate the reliability of TBCs.

A TBC system is primarily built up from four layers, namely, the ceramic top coat (TC), the thermally grown oxide (TGO), the metallic bond coat (BC), and the underlying substrate. Mismatches in the thermo-physical and mechanical properties between the four layers can lead to large residual stresses in TBCs upon the cooling process [4]. The local stress will be more complicated at a rough interface between the TC and the BC such that remarkable out-of-plane stresses appear by the undulation of the interface [5]. Moreover, the competition between growth stress in TGO and creep relaxation in all layers redistributes the stress state of TBCs [6]. Driven by local stresses, microcracks will be generated not only at the TC/BC interface but also on the TC and TGO layers [7]. During thermal cycling, these microcracks propagate and coalescence together to form a macro one [8]. Our previous study [9] found that the contest between TGO/BC interfacial crack and TC crack could accelerate the crack propagation during thermal cycling, leading to premature interfacial delamination.

Most studies have focused on the stress and failure of TBCs using two-dimensional models under simple thermal conditions (a uniform temperature change or only a temperature gradient in thickness directions, for example). However, the failure mechanisms of TBCs in gas

* Corresponding author.
E-mail address: maxf6@mail.sysu.edu.cn (X. Ma).

https://doi.org/10.1016/j.ceramint.2019.10.084
Received 1 September 2019; Received in revised form 9 October 2019; Accepted 9 October 2019
Available online 10 October 2019

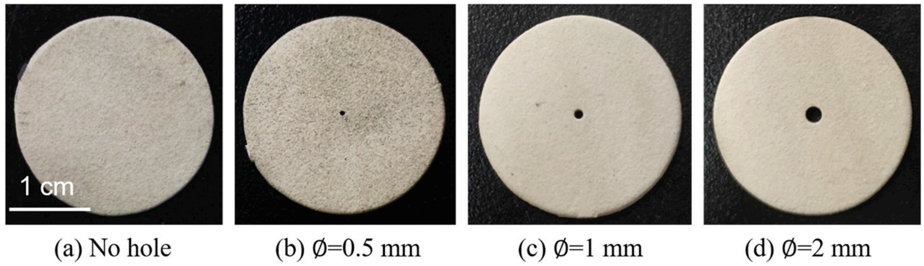

Fig. 1. As-received TBC samples with center holes of different diameters: (a) no hole, (b) hole diameter ∅ = 0.5 mm, (c) hole diameter ∅ = 1 mm, and (d) hole diameter ∅ = 2 mm.

turbine blades could be more complicated under certain operating conditions, and the effects of structure and thermomechanical loadings have to be considered [10]. In regard to the TBC-film cooling system in the gas turbine blade, although film cooling delivers outstanding cooling efficiency, it also introduces huge stress concentration around the cooling holes, increasing the likelihood of TBC failure. Kim et al. [3] found that the mixture of hot and coolant gases generated a large temperature gradient around the cooling hole, which caused additional local thermal stresses in TBCs. In our previous study [11], the temperature and stress fields in a TBC-film cooling system under certain operating conditions were numerically predicted. The results showed that the combined factors of thermal mismatch, thermal gradient, and free-edge effect around the hole aggravated the local stress state in TBCs; moreover, film cooling also produced uneven growth of TGO since the oxidation rate was related to the temperature field.

However, Li and Kang [12] found that, even without considering the effect of thermal gradient, the cooling hole could still be a stress concentrator and that deformation or cracking may occur in the oxide layer near the cooling hole during thermal cycling. Tanaka et al. [13] experimentally investigated the thermomechanical fatigue damage evolution in TBCs at a circular through hole and found surface cracks in TBCs near the hole, the direction of which was vertical to the mechanical loading. Peng et al. [14] measured the residual stress distribution in a TGO layer around a hole using luminescence piezo-spectroscopy and found that the residual stress decreased monotonically toward the hole edge, and, therefore, they speculated that the propensity for nucleating failure around holes might be reduced. However, despite the decrease in in-plane residual stress, interfacial peeling stress (normal to the interface) and shear stress could be generated simultaneously at the hole because of the free-edge effect, which may lead to Mode I and II edge cracks, respectively [2,15]. Thus, the presence of cooling hole may greatly affect the failure and lifetime of TBCs. Since the stress distributions are related to the hole geometry, the interfacial peeling and shear stresses around the cooling hole are expected to be different from those at the outer edge of the TBC samples that were studied by Hsueh et al. [2] and Chen et al. [15]. Therefore, determining the free-edge effect of cooling hole on the stress and failure in TBCs is necessary, and the effect of hole geometry should be considered.

In this work, analyses of the stress and failure in TBCs around a circular through hole under thermal cycling were conducted. The residual stress distribution on the TC along the interface was evaluated by Raman piezo-spectroscopy and finite element (FE) calculation. The vertical and interfacial cracking behaviors were examined using scanning electron microscopy (SEM), and the failure modes of TBCs around the cooling hole were determined. Moreover, the effect of hole diameter on the stress and failure of TBCs was investigated.

2. Experimental procedure

2.1. TBC samples

Before the deposition, Hastelloy-X substrates were machined into several flat disks with diameters of 25 mm and thicknesses of 1.5 mm. Center through holes, with diameters of 0.5 mm, 1 mm and 2 mm, were introduced into the substrates by an electro-discharge machining process, and the inside of the holes was polished with a diamond paste. The substrate samples without holes were also used for comparison. After grit-blasting, the substrates were deposited with 150–200 μm-thick NiCoCrAlY BCs and ~250 μm-thick ZrO_2-8 wt.% Y_2O_3 (8YSZ) TCs using an air plasma-sprayed (APS) method. The BCs were produced using NiCoCrAlY powders (Amdry 265–2, Oerlikon Metco), and the TCs were produced using 8YSZ powders (Metco 204B NS, Oerlikon Metco). After the deposition, the holes were covered with TBCs inside and were even blocked, and, therefore, they were polished using a mini electric drill to remove the TBCs on the inside of the holes. The holes were polished slowly and carefully to avoid damages to the TBCs. Finally, TBC samples with center holes of different diameters were obtained, and the as-received samples are shown in Fig. 1. The cross section of the as-received TBC samples with a hole diameter of 1 mm is shown in Fig. 2. Note that no additional coatings were covered on the inside of the hole, and no artificial microcracks were found at the hole edge.

2.2. Thermal cycling test, stress measurement and observation

Furnace thermal cycling tests were carried out for all TBC samples. Each thermal cycle consisted of a 0.15-h heat-up period, a 2-h dwell period at 1150 °C, and a 0.3-h cool-down period to room temperature. After thermal cycles were acquired, several selected samples were removed from the furnace for stress measurement and microstructure examination. At least five TBC samples for each hole diameter were chosen to evaluate the cyclic lifetime of the TBCs. For each TBC sample, the thermal cycling test was stopped when the spallation area was > 10%, and the failure time represented the TBC lifetime.

The spatial distribution of the residual stress on the TC layer was measured by Raman spectroscopy using a confocal Raman microprobe system (LabRAM HR Evolution, HORIBA) with a 532-nm laser excitation. After several thermal cycles, the samples were cut from the middle to produce cross sections after they were embedded in epoxy to ensure that the coatings remained intact. The incident beam was focused to a spot of ~3 μm on the cross section of the TC layer near the hole. The focused spot was scanned over the cross section from the hole edge, and the spectra were recorded as a function of the distance from the hole edge. The results reported in this study were the average and standard deviation from five different locations along the thickness direction at every step position. Moreover, small pieces of as-sprayed coating were scraped off as the stress-free samples, and each one was annealed in air at different times. All obtained Raman spectra were peak fitted by a mixed Lorentzian and Gaussian function. A typical example of the Raman spectrum of the TC is shown in Fig. 3. The Raman band at

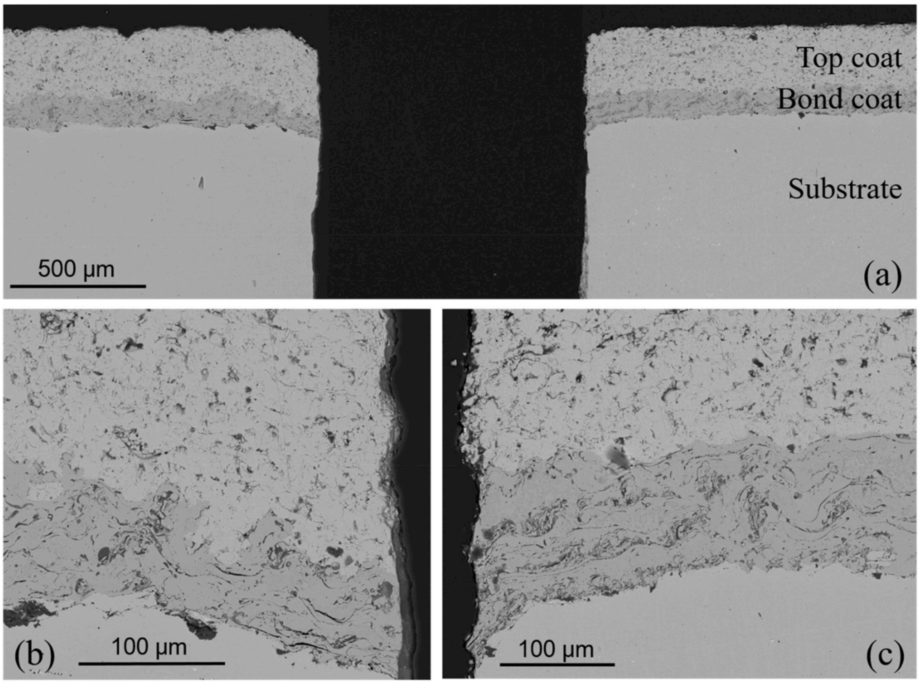

Fig. 2. SEM images of the cross section of the as-received TBC samples with a hole diameter of 1 mm: (a) overall view of the cross section of the samples, (b) morphology at the left side of the hole edge, and (c) morphology at the right side of the hole edge under high magnifications. Note that no additional coatings were applied on the inside of the hole, and no artificial microcracks were found at the hole edge.

465 cm^{-1} was chosen to evaluate the residual stress on the TC because it was well isolated from the other peaks and more sensitive to stress [16].

The coating stress measured by Raman piezo-spectroscopy is a function of the Raman peak shift relative to its unstrained state, which can be described by the following relationship [17]:

$$\Delta v = v - v_0 = \Pi_{ij}\sigma_{ij} \tag{1}$$

where Δv is the Raman peak shift from the stress-free state (v_0), Π_{ij} is the piezo-spectroscopic tensor, and σ_{ij} is the stress tensor. Since the TC is much thinner than the substrate and all interfaces are assumed flat, the normal stress to the surface is zero and the TC can be approximated under a biaxial stress state. The surface of the cross section is traction free, and, therefore, the stress component normal to the cutting plane becomes zero at the surface and increases again when going into the coating near the cutting plane. The biaxial stress, σ_B, on the TC prior to the cross section can be evaluated from Δv as follows [16]:

$$\sigma_B = \frac{1 - v_{TC}}{\Pi}\frac{E_{TC}}{E_{dense}}\Delta v \tag{2}$$

where v_{TC} is the Poison's ratio of the TC, E_{TC}/E_{dense} is the ratio between the Young's moduli of the TC and that of the fully dense YSZ, and Π is the piezo-spectroscopic constant of the dense YSZ, which is 2.01 cm^{-1}/GPa for 465 cm^{-1} [17].

Surface cracks and spallation of the samples were observed using an optical microscope (Olympus). The samples were cut from the middle to produce the cross sections after they were embedded in epoxy. After being polished, the samples were coated with gold and the cross sections were observed using a scanning electron microscope (MIRA3). The lengths of the interfacial cracks from the hole edge were quantified by image analyses using the ImageJ software.

3. Finite element model

FE models were built using ABAQUS to calculate the in-plane residual stresses and the interfacial peeling and shear stresses of the TBCs

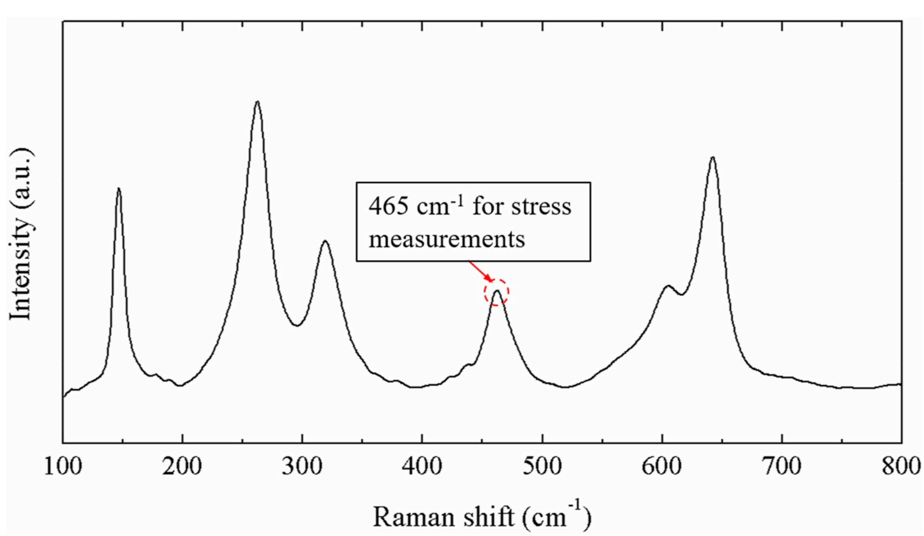

Fig. 3. Typical Raman spectrum of tetragonal ZrO_2. The shift of the Raman peak at 465 cm^{-1} was chosen to evaluate the residual stress on the TC.

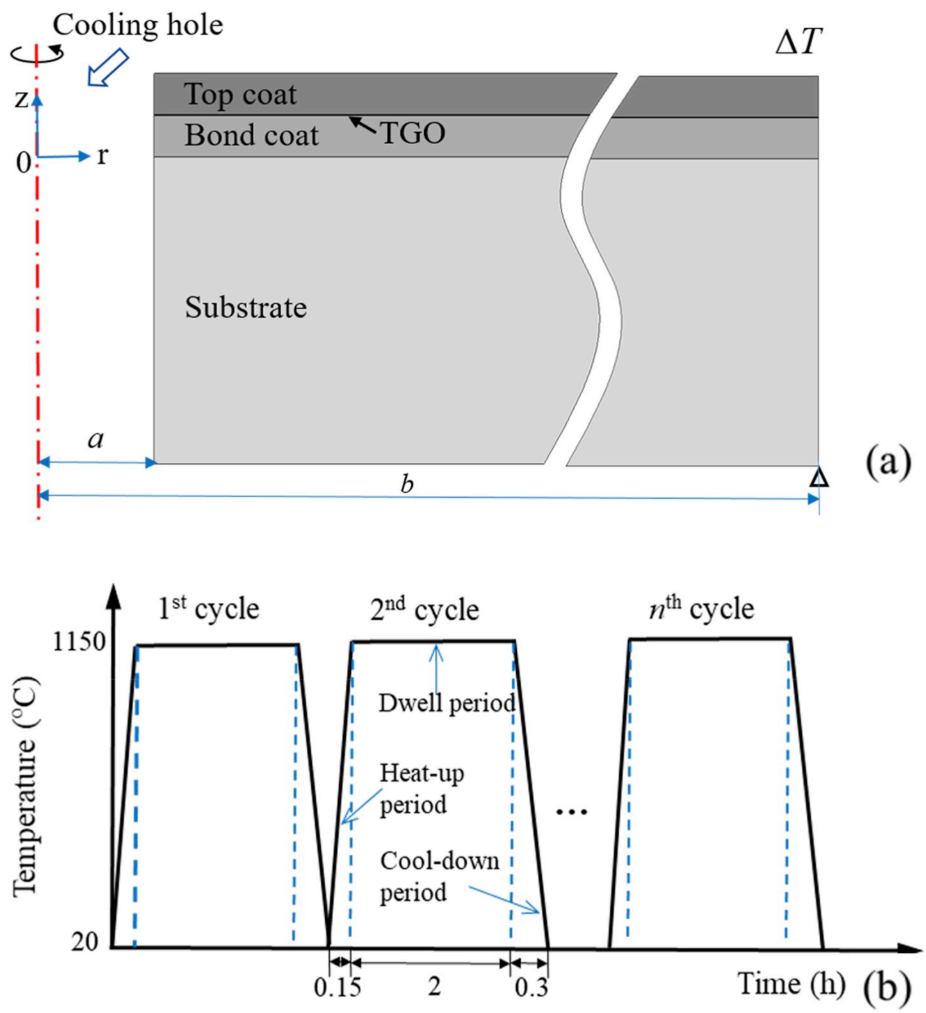

Fig. 4. Finite element model for calculation: (a) the two-dimensional axisymmetric model; (b) the thermal history.

with cooling holes. The disk-shaped TBC sample underwent uniform thermal loading without other external loadings. Considering the symmetric geometry and thermal loading, we simplified a three-dimensional model into a two-dimensional axisymmetric model, as shown in Fig. 4a. The thicknesses of all layers were kept the same as those of the experimental samples. The thickness of the TGO layer grew during the thermal cycling. The hole radius, a, was set to 0.25 mm, 0.5 mm, and 1 mm for the TBC samples with different hole diameters, and the radius of the model, b, was set to 12.5 mm so that $b \gg a$. The bottom of the outer edge of the model was restricted to move in the z direction, whereas the hole edge, outer edge, and top and bottom surfaces of the model were free from any constraints. Eight-node axisymmetric thermally coupled quadrilateral elements (CAX8T) were generated for FE meshing. The meshes in regions adjacent to the hole and all interfaces were refined to obtain sufficient accurate results. The model was considered in a homogeneous temperature field during thermal cycling, and the thermal history is shown in Fig. 4b, which was the same as in the experimental procedure.

The ceramic TC layer was treated as an elastic material, whereas the other layers were treated as elastoplastic materials, the constitutive relations of which were described by an ideal elastoplastic model. At high temperature, creep relaxation occurred in all materials. The creep behavior of all layers was described by Norton's law, expressed as follows:

$$\dot{\varepsilon}_{cr} = B\sigma^{n} \tag{3}$$

where $\dot{\varepsilon}_{cr}$ is the creep strain rate, σ is the stress, and B and n are the temperature-dependent material properties. The temperature-dependent thermal and mechanical properties including the creep parameters of all layers can be found in our previous study [9].

The TGO layer grew in thickness at the interface between the TC and the BC during the dwell time of the thermal cycling. Fig. 5 shows the experimental results of TGO growth with thermal exposure time. The thickness of the TGO layer h_{TGO}, increased with time at a decreasing rate, which could be modelled by a parabolic equation, as follows [18]:

$$h_{TGO} = k_p \cdot (t_{T\,max})^{n} \tag{4}$$

where $t_{T\,max}$ is the dwell time at the maximum temperature, and k_p and n are the oxidation coefficient and exponent, respectively, the values of which are obtained as 1.0028 $\mu m/h^n$ and 0.4, respectively, by fitting the experimental data. The lateral growth of TGO was not considered in the FE model, whereas the TGO growth in thickness was simulated by the swelling option in ABAQUS and the decreasing swelling rate was described by the CREEP subroutine [9].

4. Results

4.1. Experimental observation on TBC failure

Fig. 6 shows the spallation of TBCs with different hole diameters after thermal cycling. TBC spallation was found in regions around the outer edges in most samples, which was consistent with the previous experimental results of samples without holes [19,20]. Owing to the

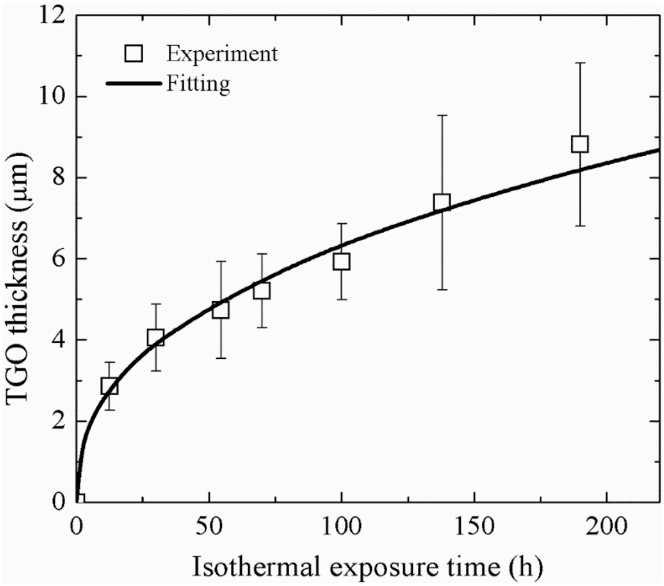

Fig. 5. Relation between average TGO thickness and thermal exposure time.

free-edge effect, interfacial microcracks were generated more easily from the hole edge, followed by continual propagation during thermal cycling, ultimately resulting in TBC spallation from the outer edge. However, as shown in Fig. 6d, TBC spallation was also found in regions around the hole in a few samples with a diameter of ∅ = 2 mm, like with the few samples with a diameter of ∅ = 0.5 mm and 1 mm, which may be driven by the local stresses at the holes. Detailed analyses will be carried out in the Discussion section.

Although TBC spallation hardly occurred in regions around the holes for most samples, surface cracks on the TCs and interfacial cracks between the TC and the BC were found near the holes after thermal cycling, which raised the possibility of TBC failures around the holes under longer thermal cycling. As shown in Fig. 7, after 95 thermal cycles, three or more surface cracks on the TCs initiated and propagated from the hole edge for the samples with three types of hole diameters. Since there were no external loadings and the thermal loading was spatially uniform, the locations of crack initiation at the hole edges were random. In the sample with a diameter of ∅ = 2 mm, the surface crack was longer and the crack mouth opened wider than in other samples, which means that larger holes generated surface cracks more easily.

Fig. 8 shows the interfacial crack patterns in the sample with a diameter of ∅ = 0.5 mm after 95 thermal cycles. It can be seen that interfacial cracks were generated at both the outer edge (see Fig. 8b) and the hole edge (see Fig. 8c) of the sample, which were mainly because of the free-edge effects of the outer edge and the hole edge, respectively. The long interfacial crack was the result of the coalescence of microcracks. During thermal cycling, microcracks mainly initiated on the TC near the interface and propagated nearly horizontally, and some might have penetrated through the TGO layer to link together to form a bigger one. The interfacial crack patterns in this sample were similar to those with a diameter of ∅ = 1 mm or 2 mm.

Fig. 9a summarizes the average edge-crack lengths at the interfaces after 95 thermal cycles for samples with different hole diameters. Only the cracks nearest to the hole edge or outer edge were counted, and the cracks far away from the edges were not considered. Since the crack lengths were counted from the cross sections produced by cutting the samples from the middle randomly, the data showed large dispersity, although they could still distinguish the differences between samples with different hole diameters. The interfacial crack at the hole edge was nearly twice as long as those at the hole edges, which makes TBC spallation more likely to occur at the outer edges. The average edge crack lengths (~1100 μm) at the hole edges showed a tiny difference for ∅ = 0.5 mm and 1 mm; however, the crack length (1520 μm) for ∅ = 2 mm was larger than the other crack lengths.

Fig. 9b presents the cyclic lifetimes of TBC samples with different hole diameters. TBCs without holes had longer lifetimes (112 thermal cycles on average) than those with holes. The cracks around the holes, including interfacial and surface cracks, led to local spallation of TBCs, and a few might even have linked with the cracks from the inside and outer edges, resulting in a large spallation area. Thus, the presence of a hole structure shortened the lifetime of TBC samples. Furthermore, the samples with a diameter of ∅ = 2 mm had the shortest lifetimes (95 thermal cycles on average) since they had the longest surface and interfacial cracks (see Figs. 7c and 9a) during thermal cycling and had the greatest potential to generate local spallation around the holes (see Fig. 6d for example).

4.2. Stress assessment

The cracks around the holes are believed to be driven by local stresses; thus, stress distributions were evaluated by Raman spectroscopy and FE calculations. Fig. 10 shows the in-plane residual stress distributions on the TCs along the interface in different samples after 50 thermal cycles. The stress distribution for the sample with a diameter of ∅ = 1 mm was experimentally measured. The FE results showed good agreement with the experimental results, which reflects the effectiveness of the FE models. In regions far away from the edges, the compressive residual stresses (roughly −105 MPa) were independent of the positions and hole diameters for both experimental and FE results. Owing to the Saint-Venant principle, this stress was almost the same as those in TBCs without holes, which can be analytically calculated according to Hsueh's solutions [2,21], and the details are presented in Appendix A. By analytical solutions, the calculated average stress on the TC was −118 MPa. This elastic solution is slightly higher than the FE and experimental results because the plasticity of all layers and the thermal cycling effect were not considered.

In both the FE and the experimental results, the residual stress decreased strikingly to nearly zero when the position moved to the hole edge. When the distance from the edge was less than 800 μm, the stresses measured by the experiments were slightly smaller than those calculated using an FEM, probably because only a few micro-cracks were generated near the hole, partly releasing the local stresses. As seen from the FE results, the residual stresses decreased more sharply for the

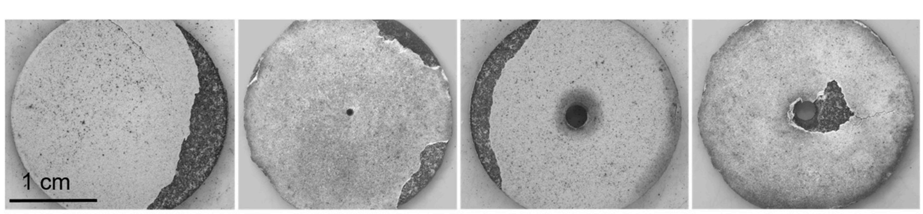

(a) No hole (b) ∅=0.5 mm (c) ∅=2 mm, sample 1 (d) ∅=2 mm, sample 2

Fig. 6. Spallation of TBCs with different hole diameters after thermal cycling: (a) no hole, after 110 cycles; (b) hole diameter of ∅ = 0.5 mm, after 100 cycles; (c) sample 1 with a hole diameter of ∅ = 2 mm, after 97 cycles; (d) sample 2 with a hole diameter of ∅ = 2 mm, after 102 cycles.

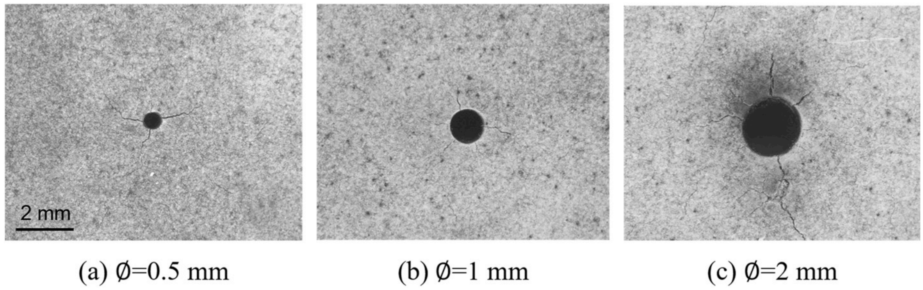

Fig. 7. Top views of the surface cracks around the holes in TBCs with different hole diameters after 95 thermal cycles.

samples with smaller holes. In addition, the stress distribution near the outer edge (the dotted line in Fig. 10) followed quite a similar trend to those near the hole, although the variation remained smoother.

Although the in-plane residual stresses decreased near the hole, the interfacial peeling stress (normal to the interface) and shear stress arose simultaneously around the hole because of the free-edge effect, which could lead to crack initiation in TBCs. Fig. 11 shows the distributions of interfacial peeling stress (σ_z) and shear stress (τ_{rz}) at the TC/TGO interface in samples with different hole diameters after 50 cycles. Both σ_z and τ_{rz} were found to be concentrated at the hole edge; however, after rapid and significant variations, they decayed to negligible values when $r > 800\ \mu m$. In Fig. 11a, σ_z changed from tensile states to compressive states and then back to tensile states. Since no external loadings were applied normal to the interface, the resultant force derived from the compressive peeling stresses was equivalent to that from the tensile peeling stresses. In Fig. 11b, τ_{rz} always changed signs from positive to negative and then decayed to zero in positions far away from the hole edge. Furthermore, both σ_{zz} and τ_{rz} were affected by the hole diameter. Although the tendencies for both σ_{zz} and τ_{rz} remained consistent, their magnitudes increased as the hole became larger.

5. Discussion

5.1. Driving forces for cracks at the hole

In the thermal cycling tests, although local spallation of TBCs hardly occurs in regions around the holes at the failure times for most samples, two types of cracks, namely, surface crack on the TC (see Fig. 7) and interfacial crack (see Fig. 8), are generated near the holes during thermal cycling. These cracks are believed to be driven by local stresses in regions around the holes. Owing to the combined factors of thermal mismatch between layers and the free-edge effect at the hole edge, the local stress state is more complicated than that in regions far away from the hole. As illustrated in Fig. 12a, in the TBC system near the hole, not only σ_z and τ_{rz} but also σ_θ is generated. These stresses (σ_z and τ_{rz}) will lead to Mode I and II interfacial cracks initiated from the hole edge, as shown in Fig. 12b. Moreover, in some periods of thermal cycling, σ_θ is in a tensile state in the region near the hole edge and upper surface of the TC, which results in the initiation of vertical cracks on the TC from the hole edge, as shown in Fig. 12c. In the TBC system, which type of crack initiates first mainly depends on the magnitudes of the local stresses and the fracture toughness, matching that between the TC layer and the TC/BC interface. When the TC and BC layers are weakly bonded, interfacial cracks may initiate first owing to the low interfacial fracture toughness; when the TC layer has a lower fracture toughness, a vertical crack is more likely to initiate first on the TC. In some cases, both interfacial and vertical cracks may occur simultaneously near the hole, as shown in Fig. 12d. During thermal cycling, both cracks propagate and even link together in regions remote from the hole, finally resulting in local spallation near the hole, as shown in Fig. 6d for example. It worth noting that, since they have the longest interfacial and surface (vertical) cracks during thermal cycling owing to the largest local stresses near the hole, the TBCs with a diameter of $\varnothing = 2$ mm have the maximum likelihood of forming local spallation near the hole.

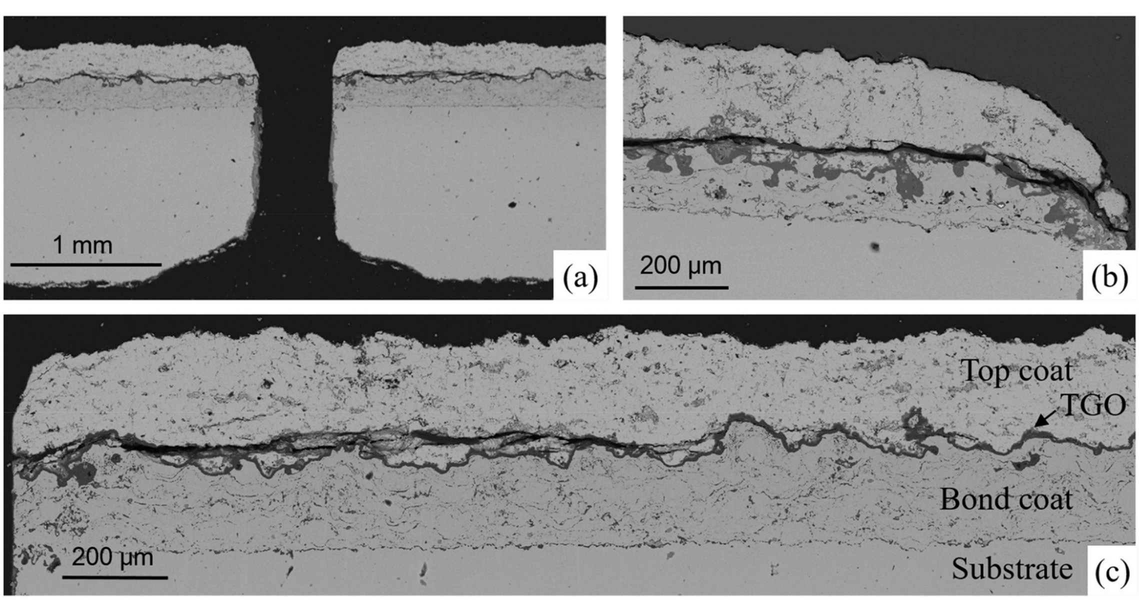

Fig. 8. SEM images of the cross sections of a TBC sample with a hole diameter of 0.5 mm after 95 thermal cycles: (a) overall view of the cross section of the TBC sample and high-magnification images showing the interfacial cracks at (b) the outer edge and (c) the hole edge of the TBC sample.

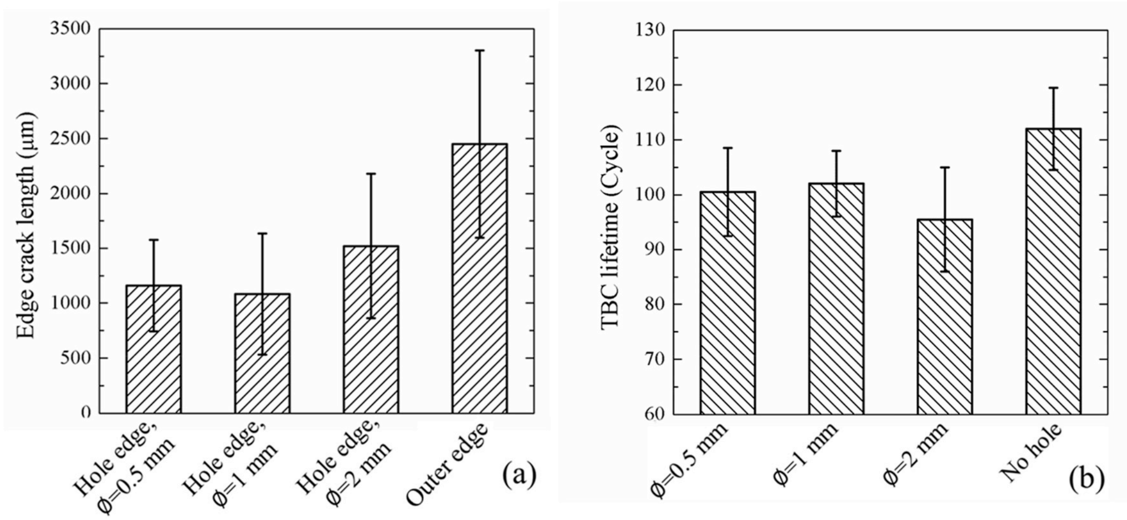

Fig. 9. Information on the (a) edge-crack lengths at the interfaces after 95 thermal cycles and (b) lifetimes of TBC samples with different hole diameters.

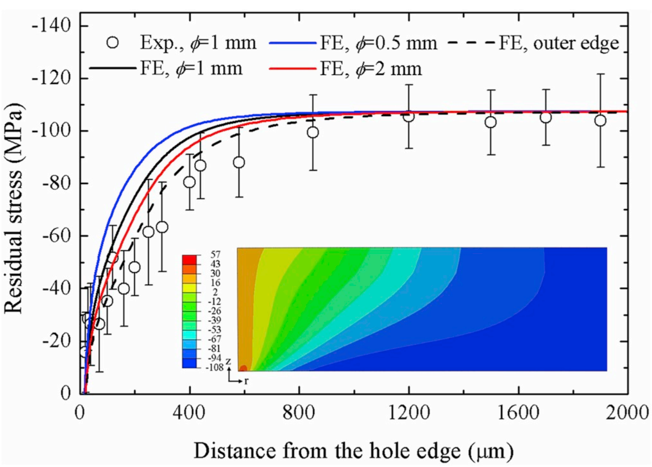

Fig. 10. In-plane residual stress distributions on the TCs from the hole edges along the interface in samples with different hole diameters after 50 thermal cycles.

5.2. Interfacial peeling moment and shear force

We now focus on the interfacial stresses and cracks in TBCs near the hole. As shown in Fig. 11, both σ_z and τ_{rz} are concentrated near the hole edge. However, the stresses vary rapidly and reverse signs in small regions. Especially for σ_z, the tensile stress only appears at the hole edge in quite a narrow region and its effect on Mode I interfacial crack is unclear. Furthermore, it is worth noting that the magnitudes of the stresses at the hole edge may be subject to errors because of the stress singularity problems [22]. It has been proposed by Moore [23] and Hsueh et al. [2] that the interfacial peeling moment and shear force derived from the local σ_z and τ_{rz} are better at characterizing Mode I and II edge cracks, respectively. In Fig. 11a, the combination of the tensile and compressive σ_z with a lever arm between them gives rise to a peeling moment. In Fig. 11b, the integral of τ_{rz} gives rise to a shear force.

A disk-shaped and multilayered TBC system model with a center hole was built to calculate the peeling moment and shear force. The cylindrical coordinate system and the numbers of layers and interfaces of the model are consistent with Fig. 1A. At interface k ($1 \le k \le n$, the interfaces between the layers are sequentially numbered by $k = 1$ to n, and interface 1 lies between layer 1 and the substrate), the peeling moment, $\hat{M}_p^k$, resulting from the peeling stress, σ_z^k, is expressed as [24].

$$\hat{M}_p^k = \int_0^{2\pi}\int_a^{\zeta} \sigma_z^k (r-a)\cdot r dr d\theta = \int_a^{\zeta} \sigma_z^k (r-a)\cdot 2\pi r dr \tag{5}$$

and the shearing force, $\hat{V}^k$, resulting from the shear stress, τ_{rz}^k, is expressed as

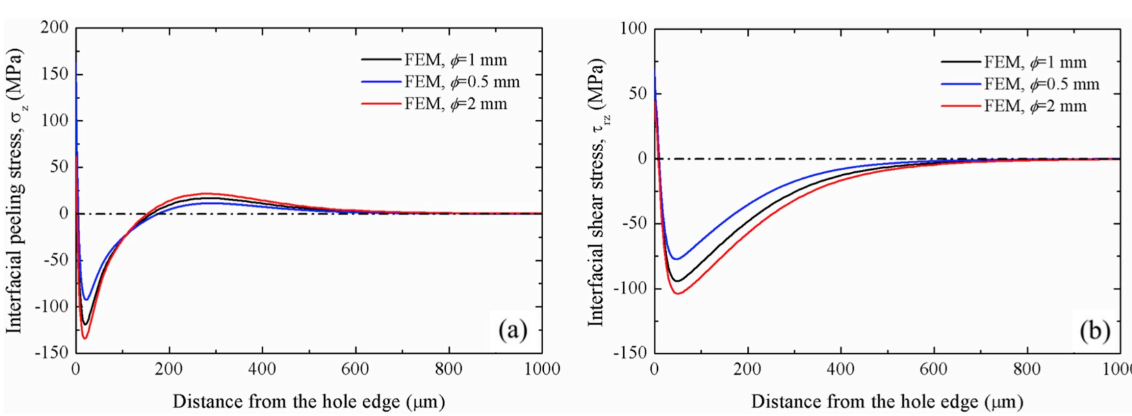

Fig. 11. FEM results of the distributions of (a) interfacial peeling stress (σ_z) and (b) shear stress (τ_{rz}) at the TC/TGO interfaces from the hole edges in samples with different hole diameters after 50 thermal cycles.

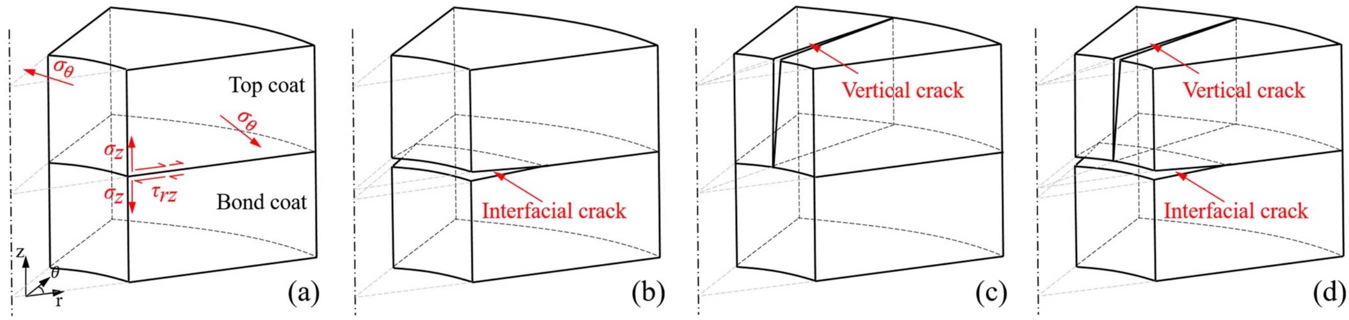

Fig. 12. Schematic diagrams of the driven forces and crack modes of TBCs in the region around the hole: (a) stress components; (b) interfacial crack driven by the interfacial peeling stress (σ_z) and shear stress (τ_{rz}); (c) vertical crack (namely, the surface crack on the TC) driven by the tensile circumferential stress, σ_θ, applied in the region near the hole edge and upper surface of the TC; (d) both interfacial and vertical cracks at the hole edge.

$$\hat{V}^k = \int_0^{2\pi}\int_a^{\zeta} \tau_{rz}^k \cdot rdrd\theta = \int_a^{\zeta} \tau_{rz}^k \cdot 2\pi rdr \tag{6}$$

where a is the hole radius and ζ is the position where $\hat{M}_p^k$ and $\hat{V}^k$ become zero. Therefore, M_p^k and V^k per unit of circumferential length in the region of the hole edge are respectively calculated by

$$M_p^k = \frac{\hat{M}_p^k}{2\pi a} = \frac{1}{a}\int_a^{\zeta} \sigma_z^k (r-a) rdr \tag{7}$$

and

$$V^k = \frac{\hat{V}^k}{2\pi a} = \frac{1}{a}\int_a^{\zeta} \tau_{rz}^k rdr \tag{8}$$

The distributions of σ_z^k and τ_{rz}^k at interface k can be obtained by FE calculations, as shown in Fig. 11 for example. Therefore, M_p and V at every interface can be calculated by Eqs. (7) and (8). Since interfacial cracks generally appear at the TC/TGO interface (see Fig. 8), attention is mainly focused on M_p and V at this interface.

Fig. 13 shows the values of M_p and V at the TC/TGO interface for samples with different hole diameters after 50 thermal cycles. M_p decreases and V increases slightly when the hole becomes bigger. However, the values of M_p are all positive for different hole diameters, which means that they are in "closing modes" and may impede the initiation of Mode I edge crack at the interface [2]. Moreover, the signs of V only indicate the shear directions and their magnitudes are concerned with Mode II edge cracking. Therefore, the TBC samples are prone to generate Mode II edge cracks at the interfaces driven by the interfacial shear forces, especially during the cooling periods of thermal cycling, and a bigger hole is more likely to generate cracks because of the larger magnitude of V.

5.3. Propagation of interfacial crack from the hole edge

The evolution of interfacial cracks driven by local stresses plays a dominant role in TBC failure around the hole. Fig. 14 shows a sketch of the propagation and coalescence of interfacial cracks in TBCs near the hole during thermal cycling. Driven by the local interfacial shear stress because of the free-edge effect, interfacial crack is prone to initiate at the hole edge first during the early stage of thermal cycling (see Fig. 14a). As thermal cycling proceeds, the edge crack propagates continuously and some interfacial microcracks begin to initiate in regions remote from the hole edge (see Fig. 14b). The microcracks are driven by the local out-of-plane stresses owing to the undulation of the interface. During the latter stage of thermal cycling, propagations of all cracks may speed up, accompanied by TGO thickening, and some may link together to form a longer one (see Fig. 14c). The local stresses in regions above the valleys of the rough interface may change from compressive states to tensile states owing to interfacial oxidation, which promotes propagation and coalescence of microcracks [25,26]. During the last stage of thermal cycling, a macrocrack is formed by the coalescence of all cracks (see Fig. 14d). The adjacent cracks may affect

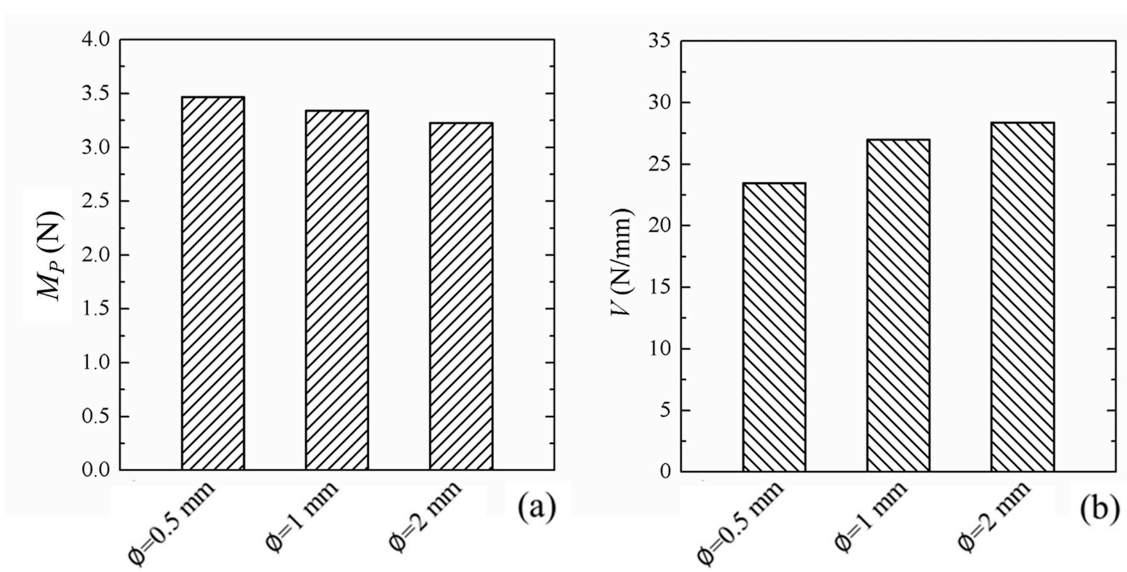

Fig. 13. Interfacial (a) peeling moment, M_p, and (b) shear force, V, at the TC/TGO interface for samples with different hole diameters after 50 thermal cycles.

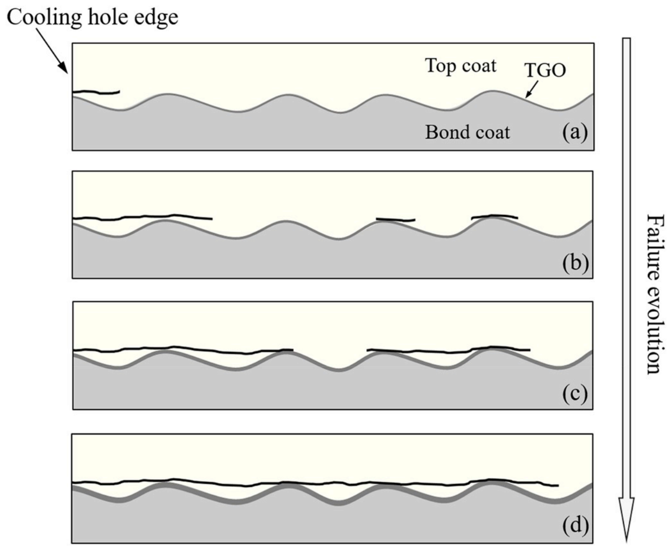

Fig. 14. Sketch of the propagation and coalescence of interfacial cracks in TBCs near the hole during thermal cycling.

each other because the stress field around one crack tip may overlap with that around another crack tip and, thus, promote crack growth and vice versa [9,27]. This mutual interaction will accelerate the crack coalescence at the interface. Finally, the interfacial macrocrack may link with the vertical cracks (surface cracks on the TC), causing local TBC spallation around the hole. Based on all above results, although film cooling technology brings about prominent film cooling efficiency, it also leads to considerable stress concentration and crack initiation around the cooling hole. Since the diameter of cooling hole greatly affects the stress and fracture behaviors of TBCs, the cooling hole might keep smaller to minimize the stress concentration for the structural and strength design of the TBC-film cooling system.

6. Summary and remarks

This study presented experimental and numerical investigation on the stress evolution and cracking behavior of thermal barrier coatings (TBCs) with cooling hole under cyclic thermal loadings. The residual stress in the top coat (TC) near the cooling hole was measured by Raman spectroscopy, and the interfacial peeling and shear stresses caused by the free-edge effect were calculated using finite element method (FEM). Two types of cracking modes near the cooling hole and their effects on TBC's lifetime were experimentally investigated. The following conclusions were obtained:

1) During thermal cycling, two types of cracks, namely surface crack in the top coat and interfacial crack, initiated and propagated from the hole edge. The coalescence of surface crack and interfacial crack led to local TBC spallation around the hole.
2) The thermal cycling test results indicated that cooling hole evidently reduced the lifetime of TBCs, i.e. from 112 cycles for original TBCs to 95 cycles for TBCs with hole diameter of 2 mm on average. Larger cooling hole led to higher local stress around the hole, which resulted in much longer interfacial and surface cracks during thermal cycling. It was consistent with the experimental observation of evident local spallation of TBCs with hole diameter of 2 mm.
3) Finite element analysis successfully reproduce the residual stress and stress distribution in multi-layered TBCs with cooling holes, with the former validated by comparison with Raman spectroscopy results. Despite the decrease of in-plane residual stress in top coating as measured, the interfacial peeling and shear stresses increased around the hole according to finite element analysis because of the free-edge effect, which act as the underlying driving force of interfacial crack initiation in TBCs. In addition, circumferential tensile stress was generated near the hole edge and the upper surface of top coat, resulting in the initiation of vertical cracks in the top coat at the hole edge.
4) Mode I and II edge cracks around the hole were analyzed using fracture mechanics method, with the interfacial peeling moment and shear force derived from the local peeling. Mode I crack along the interface at the hole edge would be impeded during the cooling stage of thermal cycling, since the interfacial peeling moment was positive and in a “closing mode”. The TBC sample was prone to generate Mode II edge crack at the interface driven by the interfacial shear force. A larger hole was likely to facilitate cracks because of larger magnitude of interfacial shear force, which indicated the importance to control the size of cooling holes.
5) The evolution of interfacial cracks driven by local stresses played a dominant role in the failure of TBCs with cooling hole. During the later period of thermal cycling, the propagation of edge interfacial cracks and the coalescence with other cracks away from cooling hole would accelerate the interfacial delamination, eventually leading to local spallation of TBCs around cooling hole.

Declaration of competing interest

The authors declare that they have no known competing financial interests or personal relationships that could have appeared to influence the work reported in this paper.

Table A1
Thicknesses and elastic material properties of all layers in the TBC system used for calculating the residual stresses.

Materials	E (GPa)	ν	α ($\times 10^{-6}$/°C)	h (mm)
TC	20	0.2	10	0.25
TGO	380	0.27	5	0.006
BC	150	0.32	15	0.2
Substrate	200	0.3	15.5	1.5

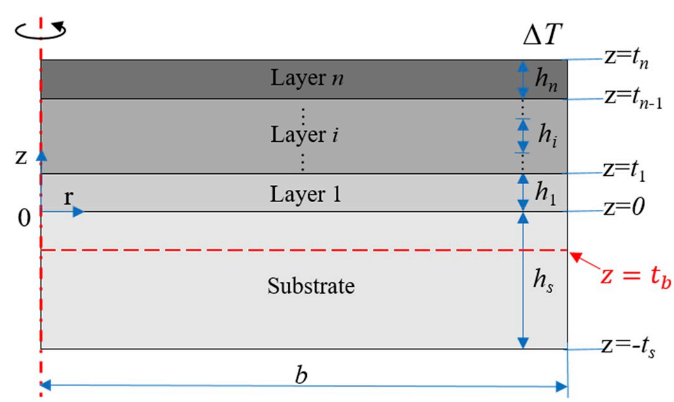

Fig. 1A. Schematic of the multilayered structure of the TBC system used for stress calculation.

Acknowledgements

This project is supported by National Natural Science Foundation of China (No. 11902370), China Postdoctoral Science Foundation (2019M653173 and 2019TQ0374), Guangdong Education Department Fund (2016KQNCX005) and Guangdong Provincial key S&T Special Project (2017B020235001 and 2019B010943001).

Appendix. Analytical solutions of the residual stresses in the disk-shaped TBC system

By the Saint-Venant's principle, the stresses around the hole have little impact on the stress distributions of the TBC system in regions far away from the hole edge. Thus, the residual stress can be calculated by a disk-shaped multilayered thin plate model without holes. Note that the calculation only considers the cool-down or heat-up period, and the oxidation and creep behaviors at dwell time are not considered. Owing to the symmetries of geometry and thermal loading, a three-dimensional model can be simplified into a two-dimensional axisymmetric model, as shown in Fig. 1A. The n layers of coating with individual thicknesses of h_i are bonded sequentially to the substrate with a thickness of h_s, and, therefore, the total thickness of the disk h_{total} is calculated by

$$h_{total} = h_s + \sum_{i=1}^{n} h_i \tag{A1}$$

The subscript i represents the number of layers of the coating, ranging from 1 to n, and layer 1 represents the layer in direct contact with the substrate. In addition, the interfaces between the layers are also sequentially numbered by $k = 1$ to n, and interface 1 lies between layer 1 and the substrate. A cylindrical coordinate system is defined to parameterize the positions within the disk such that the z-axis is collinear with the center line of the hole and the r-axis is collinear with interface 1. Hence, interface k ($k = i+1$) between layers i and $i+1$ is located at $z = t_i$, and the free surfaces of the coating and substrate are located at $z = t_n$ and $z = -t_s$, respectively.

Based on Hsueh's theory [21], under a uniform temperature change ΔT, the radial stresses in the substrate (σ_s^r) and the coating layers (σ_i^r) are respectively given by

$$\sigma_s^r = \frac{E_s}{1-\nu_s}\left(\frac{z-t_b}{\rho} + c - \alpha_s \Delta T\right) \tag{A2-a}$$

$$\sigma_i^r = \frac{E_i}{1-\nu_i}\left(\frac{z-t_b}{\rho} + c - \alpha_i \Delta T\right) \tag{A2-b}$$

where E is the elastic modulus, ν is the Poisson's ratio, α is the thermal expansion coefficient, c is the uniform strain component, ρ is the radius of the curvature, and $z = t_b$ is the location of the bending axis, where the bending strain component is zero (see Fig. 1A). For a multilayered thin disk, three parameters, namely, c, t_b and ρ, are given by

$$c = \frac{\frac{E_s h_s \alpha_s \Delta T}{1-\nu_s} + \sum_{i=1}^{n} \frac{E_i h_i \alpha_i \Delta T}{1-\nu_i}}{\frac{E_s h_s}{1-\nu_s} + \sum_{i=1}^{n} \frac{E_i h_i}{1-\nu_i}} \tag{A3}$$

$$t_b = \frac{-\frac{E_s h_s^2}{1-\nu_s} + \sum_{i=1}^{n} \frac{E_i h_i}{1-\nu_i}(2t_{i-1} + h_i)}{2\left[\frac{E_s h_s}{1-\nu_s} + \sum_{i=1}^{n} \frac{E_i h_i}{1-\nu_i}\right]} \tag{A4}$$

$$\frac{1}{\rho} = \frac{-6\left[\frac{E_s h_s \alpha_s \Delta T}{1-\nu_s}\left(\frac{h_s}{2} + t_b\right) - \sum_{i=1}^{n} \frac{E_i h_i \alpha_i \Delta T}{1-\nu_i}\left(t_{i-1} + \frac{h_i}{2} - t_b\right)\right]}{\frac{E_s h_s^2}{1-\nu_s}(2h_s + 3t_b) + \sum_{i=1}^{n} \frac{E_i h_i}{1-\nu_i}\left[6t_{i-1}^2 + 6t_{i-1}h_i + 2h_i^2 - 3t_b(2t_{i-1} + h_i)\right]} \tag{A5}$$

Note that when $i = 1$, t_{i-1} (namely, t_0) is defined as zero.

The residual stress in a four-layered TBC system can be calculated by Eqs. (A2)–(A5) by setting $n = 3$. After 50 thermal cycles, namely, 100 h of thermal exposure, the thickness of the TGO layer increases to ~6 μm. The thicknesses and elastic material properties of all layers are listed in Table A1. From Eq. (A2), the residual stress in a TC layer is a function of z and the average TC stress is calculated as −118 MPa.

References

[1] D.R. Clarke, M. Oechsner, N.P. Padture, Thermal-barrier coatings for more efficient gas-turbine engines, MRS Bull. 37 (10) (2012) 891–898.

[2] C.H. Hsueh, C.R. Luttrell, S. Lee, T.C. Wu, H.Y. Lin, Interfacial peeling moments and shear forces at free edges of multilayers subjected to thermal stresses, J. Am. Ceram. Soc. 89 (5) (2006) 1632–1638.

[3] K.M. Kim, S. Shin, H.L. Dong, H.H. Cho, Influence of material properties on temperature and thermal stress of thermal barrier coating near a normal cooling hole, Int. J. Heat Mass Transf. 54 (25) (2011) 5192–5199.

[4] A.G. Evans, D.R. Mumm, J.W. Hutchinson, G.H. Meier, F.S. Pettit, Mechanisms controlling the durability of thermal barrier coatings, Prog. Mater. Sci. 46 (5) (2001) 505–553.

[5] P. Skalka, K. Slámečka, J. Pokluda, L. Čelko, Finite element simulation of stresses in a plasma-sprayed thermal barrier coating with a crack at the TGO/bond-coat interface, Surf. Coat. Technol. 337 (2018) 321–334.

[6] J. Rösler, M. Bäker, K. Aufzug, A parametric study of the stress state of thermal barrier coatings Part I: creep relaxation, Acta Mater. 52 (16) (2004) 4809–4817.

[7] W. Zhu, Z. Zhang, L. Yang, Y. Zhou, Y. Wei, Spallation of thermal barrier coatings with real thermally grown oxide morphology under thermal stress, Mater. Des. 146 (2018) 180–193.

[8] Z. Wei, H. Cai, C. Li, Comprehensive dynamic failure mechanism of thermal barrier coatings based on a novel crack propagation and TGO growth coupling model, Ceram. Int. 44 (18) (2018) 22556–22566.

[9] J. Jiang, W. Wang, X. Zhao, Y. Liu, Z. Cao, P. Xiao, Numerical analyses of the residual stress and top coat cracking behavior in thermal barrier coatings under cyclic thermal loading, Eng. Fract. Mech. 196 (2018) 191–205.

[10] W. Zhu, J. Wang, L. Yang, Y. Zhou, Y. Wei, R. Wu, Modeling and simulation of the temperature and stress fields in a 3D turbine blade coated with thermal barrier coatings, Surf. Coat. Technol. 315 (2017) 443–453.

[11] J. Jiang, L. Jiang, Z. Cai, W. Wang, X. Zhao, Y. Liu, Z. Cao, Numerical stress analysis of the TBC-film cooling system under operating conditions considering the effects of thermal gradient and TGO growth, Surf. Coat. Technol. 357 (2019) 433–444.

[12] F. Li, K. Kang, Deformation and cracking near a hole in an oxide-forming alloy foil subjected to thermal cycling, Acta Mater. 61 (1) (2013) 385–398.

[13] M. Tanaka, C. Mercer, Y. Kagawa, A. Evans, Thermomechanical fatigue damage evolution in a superalloy/thermal barrier system containing a circular through hole, J. Am. Ceram. Soc. 94 (2011) 128–135.

[14] X. Peng, N. Sridhar, D.R. Clarke, The stress distribution around holes in thermal barrier coatings, Mater. Sci. Eng. A 380 (1–2) (2004) 208–214.

[15] L. Chen, G. Yang, C. Li, C. Li, Edge effect on crack patterns in thermally sprayed ceramic splats, J. Therm. Spray Technol. 26 (2017) 302–314.

[16] A.M. Limarga, R. Vaßen, D.R. Clarke, Stress distributions in plasma-sprayed thermal barrier coatings under thermal cycling in a temperature gradient, J. Appl. Mech. 78 (1) (2011) 011003.

[17] A.M. Limarga, D.R. Clarke, Piezo-spectroscopic coefficients of tetragonal-prime yttria-stabilized zirconia, J. Am. Ceram. Soc. 90 (4) (2007) 1272–1275.

[18] T. Beck, R. Herzog, O. Trunova, M. Offermann, R. Steinbrech, L. Singheiser, Damage mechanisms and lifetime behavior of plasma-sprayed thermal barrier coating systems for gas turbines—Part II: Modeling, Surf. Coat. Technol. 202 (24) (2008) 5901–5908.

[19] E. Altuncu, E.I. KaraalI, G. Erdogan, F. Ustel, A. Turk, The effect of samples geometry and thermal cycling test type on the thermal shock behaviour of plasma sprayed TBCs, Plasma Process. Polym. 6 (S1) (2009) S711–S715.
[20] L. Wang, C. Ming, X. Zhong, J. Ni, S. Tao, F. Zhou, Y. Wang, Prediction of critical rupture of plasma-sprayed yttria stabilized zirconia thermal barrier coatings under burner rig test via finite element simulation and in-situ acoustic emission technique, Surf. Coat. Technol. 367 (2019) 58–74.
[21] C.H. Hsueh, Thermal stresses in elastic multilayer systems, Thin Solid Films 418 (2) (2002) 182–188.
[22] C. Chung, J.W. Eischen, The free-edge stress singularity at an interface between bilinear materials, Int. J. Solids Struct. 28 (1) (1991) 105–113.
[23] T.D. Moore, Thermomechanical peeling in multilayer beams and plates—a solution from first principles, Int. J. Solids Struct. 42 (1) (2005) 271–285.
[24] J.S. Jiang, X.F. Ma, B. Wang, Stress analysis of the thermal barrier coating system near a cooling hole considering the free-edge effect, Ceram. Int. (2019), https://doi.org/10.1016/j.ceramint.2019.08.267 In press.
[25] M. Ranjbar-Far, J. Absi, G. Mariaux, F. Dubois, Simulation of the effect of material properties and interface roughness on the stress distribution in thermal barrier coatings using finite element method, Mater. Des. 31 (2) (2010) 772–781.
[26] L. Su, W. Zhang, Y. Sun, T. Wang, Effect of TGO creep on top-coat cracking induced by cyclic displacement instability in a thermal barrier coating system, Surf. Coat. Technol. 254 (2014) 410–417.
[27] J. Song, S. Li, X. Yang, D. Shi, H. Qi, Numerical study on the competitive cracking behavior in TC and interface for thermal barrier coatings under thermal cycle fatigue loading, Surf. Coat. Technol. 358 (2019) 850–857.